Bauer *et al. Journal of Electric Propulsion* (2026) 5:10
https://doi.org/10.1007/s44205-026-00182-0

Journal of Electric Propulsion

RESEARCH Open Access

Direct comparison of different probe positioning and pointing schemes for plume measurements using an Advanced Cusp Field Thruster

Leonard Bauer[1,2*], Max Vaupel[2], Hans Blättermann[2], Saskia Sütterlin[2], Gerrit Kottke[2], Franz Georg Hey[2] and Peter J. Klar[1]

*Correspondence:
Leonard Bauer
leonard.bauer@airbus.com
[1]I. Physikalisches Institut, Justus Liebig University Giessen, Heinrich-Buff-Ring 16, 35392 Giessen, Germany
[2]Airbus Defence and Space GmbH, Claude-Dornier-Straße 1, 88090 Immenstaad, Germany

Abstract
We investigate how probe positioning and pointing schemes affect ion current density measurements, specifically total beam current and divergence efficiency. Experiments were conducted using a five-axis gantry and a nude Faraday probe in the plume of an Advanced Cusp Field Thruster (ACFT). By mimicking Cartesian and spherical diagnostic geometries, we compare typical measurement strategies within a single setup. Additionally, maximizing local current via probe rotation reconstructs the ion plume origin, revealing a volumetric source shaped by the discharge chamber. While mathematical corrections for rigid probe misalignment exist, uncertainties from collector angle and secondary electron emission grow significantly with incidence angle. Results show that optimizing probe alignment to within $\pm 2°$ reduces divergence and beam current measurement uncertainty to below 2.5%. These findings highlight diagnostic geometry as a key factor in high-precision plume characterization.

Keywords Cusp field thruster, Plasma diagnostic, Gantry, Plume characterization

Introduction

Electric propulsion (EP) systems are increasingly being used in space applications, and characterizing their plasma plumes is essential to understand thrust efficiency, spacecraft interaction, and loss mechanisms [1–4]. A wide variety of diagnostic approaches employ different types of probes and movement geometries [3–26]. This range of diagnostics is essential to fully characterize EP plumes. Each diagnostic tool targets a different plasma parameter. Probes such as retarding potential analyzers and E×B probes are used to assess ion energy and ion species. Time-averaging Faraday probes are the most common tool for measuring the local ion current density in a plume, and are therefore typically used in scanning units for determining the spatial ion beam profile.

© The Author(s) 2026. **Open Access** This article is licensed under a Creative Commons Attribution 4.0 International License, which permits use, sharing, adaptation, distribution and reproduction in any medium or format, as long as you give appropriate credit to the original author(s) and the source, provide a link to the Creative Commons licence, and indicate if changes were made. The images or other third party material in this article are included in the article's Creative Commons licence, unless indicated otherwise in a credit line to the material. If material is not included in the article's Creative Commons licence and your intended use is not permitted by statutory regulation or exceeds the permitted use, you will need to obtain permission directly from the copyright holder. To view a copy of this licence, visit http://creativecommons.org/licenses/by/4.0/.

Faraday probes exist in nude, collimated, and shielded geometries. However, most studies provide little detail on the design of the probe or associated measurement uncertainties. A notable exception is the nude Faraday probe, which is well-documented and tested in various publications summarized by Brown et al. [2].

In addition to a suitable probe, each scanning unit for measuring ion beam profiles requires a movement and positioning strategy of the probe. The movement strategies used for positioning and orienting probes in spatial plume measurements remain largely ad-hoc and unstandardized. Approaches range from multi-axis gantries of varying complexity from one to five axes [3–13] to spherical systems of a single probe or a C shaped array of probes on a rotational arm [14–25]. Each approach potentially possesses distinct sources of measurement uncertainty and poses specific correction challenges. To date, there have been no publications in the literature on a dedicated comparison of different positioning and pointing schemes employing the same probe applied to the same thruster with the same operating point.

This study aims to fill this gap by using a five-axis gantry system equipped with a single nude Faraday probe based on a design published by Brown et al. [2] to compare different movement strategies, including both spherical and planar geometries. The object under test is an Advanced Cusp Field Thruster (ACFT), operated at a constant set point throughout the campaign. By effectively mimicking the geometries of different diagnostic facilities within a single setup, we assess the acquired data in terms of results and measurement uncertainty for the various movement and pointing schemes.

Section "Probe positioning strategies for plasma plume measurements" introduces the different probe positioning and pointing strategies employed in mechanisms today. Section "Experimental setup" details the hardware used, including the ACFT, the nude Faraday probe, and the gantry system. Section "Methodology" describes the data analysis and test methodology. Section "Results and discussion" presents and compares the measured data of the spatial plume scans, including a reconstruction of the ion source. Section "Conclusion" evaluates the different strategies and makes recommendations for plasma diagnostic mechanism designs.

Probe positioning strategies for plasma plume measurements

Symmetry considerations are often used to simplify probe positioning for spatial ion-beam measurements, reducing the number of positions required to characterize the beam profile. Typical assumptions regarding the ion source are:

(i) The ion source is approximated as a point source. This simplifies the geometric relationship if the characteristic size d of the emitting surface (i.e. the thruster exit plane) is much smaller than the probe distance R.
(ii) The ion source has rotational symmetry about the beam axis. This allows reducing the measurement to a single line scan through the beam center.

Many electric thrusters do indeed possess a plume profile with rotational symmetry. Examples include most gridded ion engines (GIEs) [3], Hall thrusters (HT) [1], magnetic nozzle electron-cyclotron resonance (ECR) thrusters with a rod antenna such as ONERA's MINOTOR thruster [27] or most ACFTs [28].

Depending on the acceptable threshold of the d to R ratio, assumption (i) is well fulfilled for small thrusters such as the Alberich ACFT [28] or RIT-μX [29] in a large test

chamber. However, assumption (i) is generally invalid for larger thrusters of the 3–5 kW class such as the iFACT-MP thruster [30] or the RIT-2X in most test facilities. Furthermore, it is not applicable in case of clusters of thrusters which are candidates for 20 kW class systems. Similarly, assumption (ii) is not always fulfilled. Examples are thrusters which do not possess a thruster exit plane of rotational symmetry [4, 5], or a cluster of ion thrusters which will not have rotational symmetry. Even ion thrusters that do possess rotational symmetry may require asymmetric neutralizer placement, which distorts the plume and breaks symmetry [31, 32].

Furthermore, the discharge vessels of most plasma and ion thrusters are of finite extension. Thus, the origin of an ion can be anywhere within the discharge vessel and will leave the system anywhere through its exit plane. Therefore, these ion trajectories extrapolate back to an extended region inside the discharge vessel, not a single point. Treating the source as point-like by relying on assumption (i) therefore risks systematic error. The point of intercept of the extrapolated ion trajectories may also differ from the center of the exit plane as will be discussed in Sections "Experimental setup" and "Results and discussion".

Currently, the most common diagnostic system for spatially resolved measurements is a single mechanized arm with a probe (or probe array) [14–25] where the probe is moved on hemispheres with the thruster exit-plane located in their origin. Typical measurement ranges in these publications are $\pm 80\,^{\circ}$ with angular resolutions of presented data of about $1\,^{\circ}$. However, various other gantry types are also used and reported [3–13]. Typical examples are shown Fig. 1. The four graphs depict different geometric configurations. Graph (A) and (C) show gantry systems based on Cartesian coordinates (X,Y,Z)

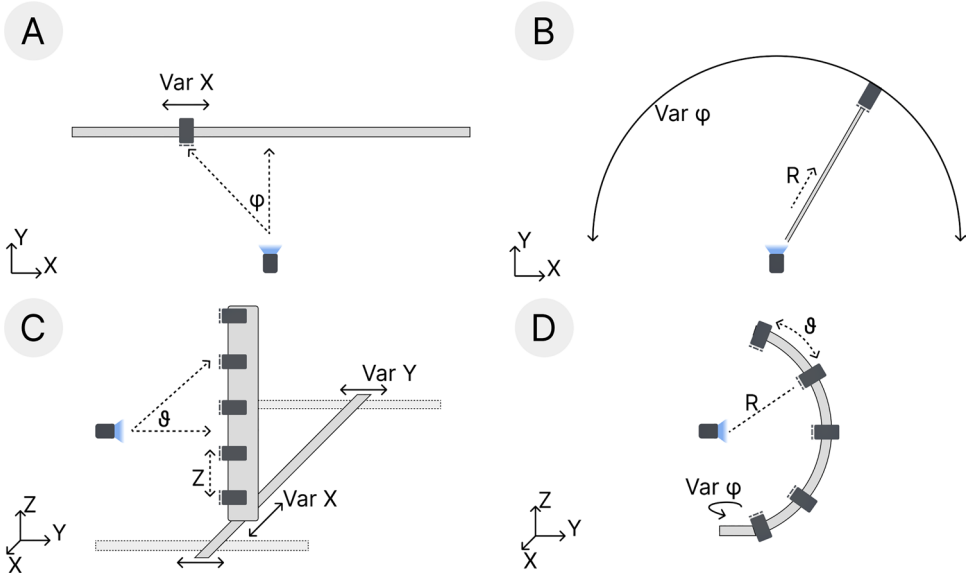


Fig. 1 Schematic comparison between the different movement and pointing strategies currently employed in electric propulsion test facilities [3–25]. The solid lines present motorized movement along a linear axis or angle rotation about an axis. Schemes A and B depict arrangements for one-dimensional scanning along an axis parallel to the thruster exit plane with variable X and on a semi-circle with radius R and variable angle φ, respectively. The Faraday probe is rigidly mounted. Schemes C and D enable a three-dimensional scanning of the Faraday probe. In C the Faraday probe is positioned making use of the three Cartesian coordinates (X,Y,Z) with the rigidly mounted Faraday probe oriented antiparallel to the Y-direction. In D the Faraday probe is positioned making use of the three spherical coordinates (R,φ,ϑ) with the rigidly mounted Faraday probe always pointing to the origin of the spherical coordinate system

for "linear" (or planar) scans whereas graphs (B) and (D) refer to systems employing spherical coordinates (R,ϕ,ϑ) for scanning on spherical surfaces.

The simplest scanning configurations are those where only one variable is varied, either in a linear sweep, e.g. with a single variable X-axis, as in graph (A) or in an angular sweep with variable ϕ as in graph (B) of Fig. 1. In both cases, the scan occurs in a plane containing the plume center (i.e., which contains the central point of the thruster exit-plane, as indicated in Fig. 1). In case of the linear scan, the measurement position where the probe points in the direction of this central point of the thruster exit-plane defines the middle of the scanning range, for all other probe positions an angle-correction for the incoming ion current density must be conducted. The effective collector area. and thus the measured current density, varies with the cosine of ϕ ($\varphi = 0\ ^\circ$ corresponds to normal incidence on the collector surface). In case of a spherical scan, the gantry must be aligned such that the probe is rotated at distance R about the central point of the thruster exit-plane (or its assumed point source). Thus, single scans with these systems yield correct beam profiles only if assumptions (i) and (ii) are fulfilled.

Gantry systems with three degrees of freedom can position the probe anywhere within a volume, providing significantly more spatial information. Measuring current distributions in multiple planes (or sphere-shells) at varying distances becomes possible and allows tracing prominent features in the spatial ion beam profile back to their origin. This "plume triangulation" assumes consistent plume structure across distances. This approach is fully independent of assumption (ii) but still relies on assumption (i).

Here, the probe orientation is fixed: either facing along the Z-direction for linear systems (Fig. 1 C) or facing the thruster center for spherical scanners (Fig. 1 D). Tracing ion trajectories back to the thruster yields a single point of convergence. This "triangulation" requires iterative correction, as the effective collector area depends on the incidence angle.

This issue is resolved by adding two additional degrees of freedom, allowing free variation of the probe's pointing direction. This is achieved via a gimbal for yaw and pitch. Such a 5-axis gantry allows the probe orientation to be optimized at every position to identify the direction of maximum ion current. Tracing back the directions found by local "current maximization" yields an extended volume inside the discharge vessel where the extrapolated paths intercept. Since the maximum current corresponds to normal incidence, the probe orientation directly defines the line of sight to origin of the impinging ions.

Experimental setup

Advanced Cusp Field Thruster

The ion source used in this study is a 300 W Advanced Cusp Field Thruster (ACFT) with rotational symmetry about the plume direction [33]. The opening diameter of the thruster exit is 35 mm. This type of thruster has been developed at Airbus since 2009 [34, 35]. The ACFT is a variant of the Cusp Field Thruster (CFT) concept from the 1960s [36]. Similar approaches are the basis of developments such as Thales' High Efficiency Multistage Plasma Thruster (HEMPT) [37] or MIT's Diverging Cusped-Field Hall Thruster (DCHT) [38]. The design, principle of operation, and performance characteristics of ACFTs are now well documented in the literature [20, 28, 30, 33–35, 39–45].

The operating principle of an ACFT is briefly summarized based on the sketch in Fig. 2. The permanent magnets (11) and (13) in conjunction with the pole shoes (12) and (15) create a strong magnetic field which confines the electrons to the central plasma region (09). The confined electrons collide with neutral particles of the gas propellant and create ions which are free to move towards the thruster exit-plane. Similar to HTs or GIEs, the ions are only accelerated near the exit plane where the acceleration potential is not shielded by the plasma. When neglecting interactions inside the plume, the ions follow straight trajectories (indicated by arrows) perpendicular to the curvature of the exit plane (10). Projecting the trajectories back in to the thruster vessel defines a point-like source of the ion-beam. When the viewing angle between probe and thruster is smaller than the opening angle of the discharge chamber (5) the lines converge inside the thruster. If the probe were to view these ions from outside this viewing angle, the ions would appear to converge at the edges of the thruster near the magnetic cusps. The exit plane is given by the boundary layer of inward and outward facing magnetic field lines and is called the separatrix and serves as a virtual grid at the exit plane [5, 46] its shape can be simulated using standard software. These cusps at the exit plane ensure that electrons can only leave or enter the thruster via collisions, and electrons inside the discharge vessel can typically only leave via the anode (08) in the back of thruster which closes the electric circuit with the cathode (01).

During the plume measurements, the ACFT was operated at 300 V and 237 mA with a krypton flow of 0.5 mg/s. The power output was controlled by a FUG MCA 3000–3000 and the mass flow is controlled with a MKS GE50A013501MBV020. Minor thermally induced long-term drifts of the discharge behavior were corrected during data analysis by normalizing the measured ion current on the probe by the anode current. A LeCroy WR2044 oscilloscope and CP031A current probe were used to ensure that no short term instabilities occurred during the measurements. The hollow cathode for beam

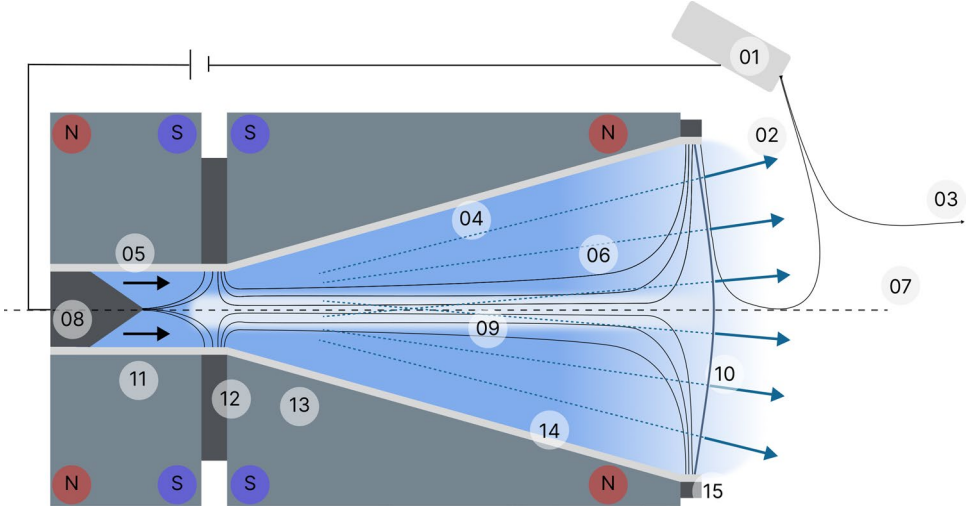


Fig. 2 Schematic image of an ACFT, with the cathode (1), the ions that leave the thruster (2), the electrons that leave the cathode to follow the beam (3), the projected origin of the ions inside the thruster (4), the neutral gas entering the discharge chamber (5), the magnetic field lines and path of the electrons inside the thruster (6), the thruster center line (7), the anode (8), the central, high density plasma region (9), the separatrix (10), the feed magnet (11) the ferromagnetic Pole shoe (12), the exit magnet (13), the ceramic discharge chamber (14) and the front Pole shoe (15). Magnetic orientations of the two magnets are shown as N for north and S for south, the coordinate system of the rotationally symmetric thruster is omitted, the only relevant directions are parallel and perpendicular to the thrust axis

neutralization is a separate device. It uses 0.122 mg/s of krypton during operation. The background pressure during operation of the ACFT thruster system remained below 3×10^{-5} mbar (nitrogen equivalent) as measured by a Pfeiffer PBR 260. It was maintained by a turbo-molecular pump, a cryogenic pump, and a cold trap.

5-Axis gantry

The gantry, which is used to position and point the nude Faraday probe in this study, has three translational axes (X, Y, and Z) as well as yaw (ϕ) and pitch (ϑ) rotational axes of the gimbal mount of the Faraday probe. This allows the probe to be positioned and pointed virtually anywhere in the vacuum chamber. This setup, as shown in Figs. 3 and 4, is similar to (C) from Fig. 1 where the vertically stacked probes along the Z-axis are replaced by a motorized Z-axis with a single probe on a gimbal mount pivoting into both ϕ and ϑ. The zero point of each axis is the center of the exit plane of the thruster, where Y becomes negative behind the thruster, X becomes negative to the left of the thruster and Z becomes negative below the thruster.

All five axes are driven by Phytron stepper motors and mechanically coupled. Microstepping provides 20,000 steps per full rotation which is controlled with a Phymotion motor controller. The cables connecting the motors to the controller are individually shielded. The Y-axis employs a timing belt with a floating-side sled to accommodate chamber deformation during pump-down and has a range of −50 to 1000 mm relative to the thruster. The X-axis is vertically stacked onto the Y-axis, moves via a rack-and-pinion drive and has a range of −500 mm to 500 mm relative to the thruster. Both the X and the Y-axis use dry ceramic-ceramic ball bearings and can move at 10 cm/s. The vertical Z-axis is built against a tower moved by the X-axis. It has a range of −200 mm to 300 mm relative to the thruster. It moves via a lead screw and low-outgassing polymer

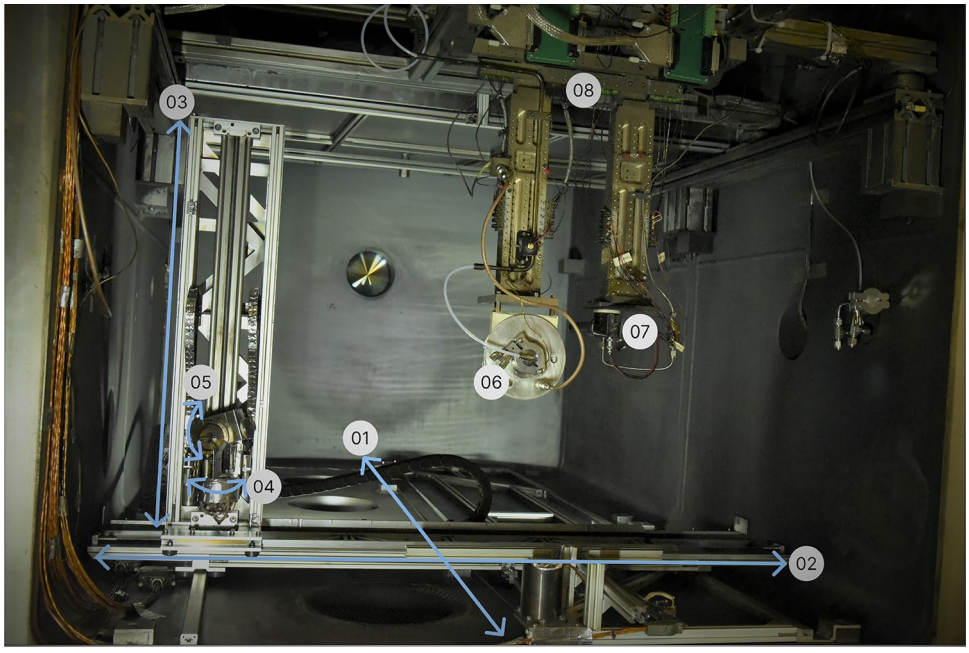


Fig. 3 Annotated photograph of the test setup in the Airbus Micro Newton test facility. The three linear axes Y-X-Z (01–03) carry the gimbal with the two angular axes (Yaw-Pitch, 04–05). The 300 W ACFT (06) and a hollow cathode (07) are attached to the two arms of the double pendulum (08). To increase the accuracy of the relative thruster - gantry position both pendulums are locked in place

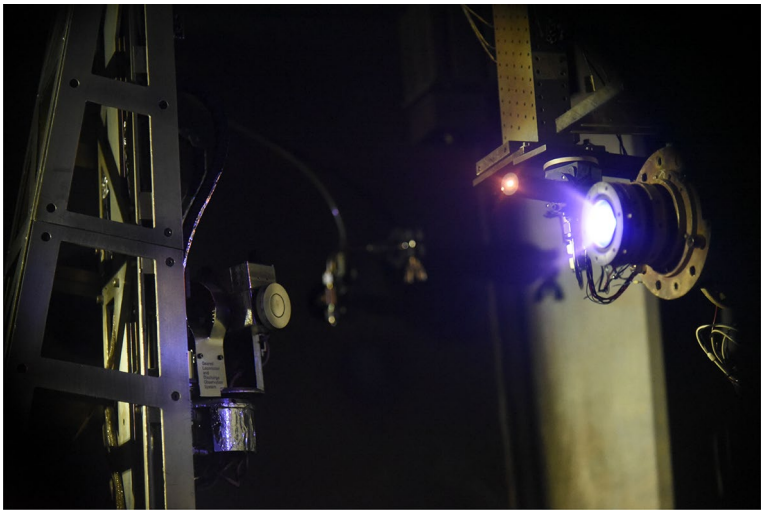


Fig. 4 Photograph of the test setup during the experiment. The tower of the vertical gantry axis with the gimbal in the center is shown on the left. Thin aluminum sheets protect the two gimbal motors and gears from ion bombardment. The collector and its guard ring point towards the thruster located on the right. Thruster and neutralizer are attached to the thrust balance of the Airbus Micro Newton test facility

linear bearings at a velocity of 1 cm/s. The limiting factor of the movement speed generally is the acceleration, which is kept low to minimize the jerk onto the gimbal of the yaw and pitch axes. All three translatory axes use Phytron VSS 56 stepper motors.

The gimbal mount uses brass gears to increase the effective torque output of the Phytron VSS 25 stepper motors and cabling is routed through the central bearing axis to eliminate torsional forces. This results in a −90 ˚ to +90 ˚ range in the yaw direction and −42 ˚ to +50 ˚ in the pitch direction. All axes are homed using magnetic proximity sensors. A laser diode verifies the gantry-thruster alignment prior to and after pump-down which ensures co-linearity within0.25 ˚ and 0.25 mm. Spatial deviations from floor tilt (up to 2 ˚ and up to 4 mm) are mapped beforehand and are used to correct commanded movements. The gantry is optimized to utilize the maximum possible volume inside the vacuum chamber and can reach as close as 125 mm to its side walls, as well as 85 mm above its floor.

Pointing and positioning accuracy of the mounted Faraday probe was assessed using a laser diode in place of the collector, aimed at reference targets located at the position of the thruster. This configuration verifies if the combined 5 axes of the gantry align with the thruster's physical location. Effectively, it determines the target size required to ensure that the laser always hits target in place of the thruster. A 10 mm target sphere was accurately targeted in 90% of all probe positions, and a 15 mm target could be hit from all probe positions. This yields a conservative positioning and pointing uncertainty estimate of 7.5 mm. Gear backlash was not resolvable in test and is considered negligible within the other tolerances.

A value of 7.5 mm for the combined positioning and pointing accuracy is a high uncertainty for a five axis mechanism when compared to systems made for metal machining or general metrology equipment, and upgrading the gantry with optical trackers could decrease the total mechanical uncertainty by an order of magnitude. With the system shown in this publication we can assume deviations between the assumed plume origin

and the actual origin of more then 7.5 mm to be resolvable, which was deemed sufficient given the diameter of the opening at the exit plane of 35 mm.

Since previous publications have not disclosed their values, the accuracy of our gantry system cannot be compared to other plasma diagnostic systems. While Brown et al. [2] recommends 0.5% of R, this value is unlikely to be reached in practice since it also represents the limit of machining tolerances of a single solid part of typical plasma diagnostic dimensions [47] and not the assembly and alignment tolerances of a movement mechanism, a probe mount and a thruster, which may be mounted individually on a separate thrust balance assembly. Whether or not the discussion on the alignment accuracy as well as the point source validity is omitted in previous works is due to it being unknown or because the system design justifies this omission remains unclear [3–26].

The thruster and the 5-axis gantry system equipped with the nude Faraday probe were installed in the Airbus Micro Newton test facility as shown in Figs. 3 and 4 from different directions to provide an overview of the setup.

Nude Faraday probe

As detector for ion density measurement and as the payload of the gantry, we use a nude Faraday probe following the design of Brown et al. [2]. The design of this Faraday probe with guard ring allows robust measurements in a simple geometry. The collector of our nude Faraday probe is a 17 mm aluminum plate which is surrounded by a 34 mm guard ring, mounted in a boron nitride holder. Key features like vent holes and isolator layout match the reference design by Brown. Central collector and guard ring are electrically isolated from one another and their bias voltage is set to −32 V relative to the common ground of thruster, gantry and cathode. This bias voltage is experimentally determined in accordance with the publications of Brown et al. and Blättermann et al. [2, 45] and is kept fixed for all positions. The probe is connected to a Keithley 2401 source meter via shielded coaxial cabling. During operation, the system achieves a signal-to-noise ratio of ≈ 100 across a current range of 1 nA to 1 mA, with typical repeatability within ±1 %. This value is limited by the electromagnetic noise introduced by the shielded stepper motor harness. The internal integration time of the source meter is set to 0.01 s, 1 to 2 orders of magnitude longer than the typical oscillation periods of the ACFT used.

The bias voltage of the Faraday probe also attracts low-energy ions, especially those arising from background pressure related facility effects such as CEX or partial neutral ingestion near the thruster exit. It should be noted that, although the nude probe does not block low-energy ions, its geometry enables a systematic correction of these effects during post-processing [2, 48]. It is therefore recommended that measurements with such a probe are carried out for various background pressures, measurement distances, and thruster operating conditions in order to be able to quantify the impact of low-energy ions on the measurement results.

However, in our comparison we do not aim to characterize a thruster unit; we aim to compare the different probe pointing schemes which natively arise from the commonly used probe positioning schemes. As a result we do not distinguish contributions from slow and fast ions. For either positioning scheme the vacuum and thruster conditions are essentially constant apart from a slight change in pumping speed and therefore background pressure between the linear and the spherical measurement campaign, likely due

to onset of saturation of the cryogenic pump. This will be discussed in Sections "Results and discussion" and "Conclusion".

Methodology

Probe positioning and pointing schemes

Following the recommendations of Brown et al. [2] we measure the spatial ion beam current distribution in several planes at different distances from the center of the thruster exit-plane. In total, we study two different scanning schemes each with different subschemes for pointing the Faraday probe.

The first scanning scheme "Linear" (L) is based on Cartesian coordinates (see Fig. 1 A and C). The thruster-exit is centered at the origin of the Cartesian coordinate system with the nominal beam direction along the Y-axis. Three scans are performed in the (X,Z) planes at distances of Y = 150 mm, 250 mm, and 350 mm, respectively. The spatial resolution is given by 25 mm between two measurement positions in the plane. The plane itself spans all the way from one side wall of the square vacuum tank to the other. This leads to a variable angular resolution and range which depends on the distance from the thruster. For this positioning scheme, three different pointing schemes are employed:

(L-1) Rigid Faraday probe: The normal of the detection area is antiparallel to the Y-direction at all positions. A correction of the effective detection area is applied by multiplying by the cosine of the effective angle, requiring assumption (i).
(L-2) At each scan position, the Faraday probe points towards the center of the thruster exit plane as determined mechanically by laser pointing prior to pump down. No additional correction is necessary. The underlying assumption is the same as in (L-1), but measurements at high effective angles will capture the nominally largest current signal. Thus, measurement uncertainty in (L-2) should be reduced compared to (L-1).
(L-3) At each scan position, the direction of the impinging ions is determined by maximizing the current signal of the Faraday probe by varying pitch and yaw angle of the probe in the vicinity of the nominal direction, requiring no prior assumption of the origin of the ion trajectories impinging on the collector surface.

The data from each pointing scheme is analyzed self-consistently. If the plume origin triangulated via the three planes changes from the initially assumed thruster exit plane, a correction for the new effective angle, distance, and collector surface area is applied and the method is repeated iteratively. The spatial resolution is given by 25 mm between measurement locations within a plane and a distance of 100 mm between two planes.

The second scanning scheme, "Spherical" (S) is based on spherical coordinates (R, ϕ, ϑ) with the origin in the center of the thruster exit plane. Here, the angular the resolution is set to 2° between measurement locations within a plane and 100 mm between two planes.

(S-2) corresponds to pointing scheme (L-2). Pointing scheme (L-1) has no meaningful spherical counterpart. As in the (L-1)-scheme, a triangulation approach can be used in the (S-2) scheme in order to yield the intersection point of the back-traced ion trajectories consistent with the point-source assumption. Again, if there are minor misalignments between the nominal direction and the direction of the back-interpolated intersection, the change in effective surface area and the SEE incidence angle

are corrected by an iterative approach. Since these effects scale to the cosine of the effective angle, their impacts are minor.
(S-3) seeks the maximum ion current at each location by varying the orientation of the Faraday probe as described above analogously to (L-3).

Data analysis

The data analysis of the local ion currents measured by the nude Faraday probe is based on well-established models for far-field measurements [2], but is also affected by the positioning with respect to the thruster. Specifically, the measured current I, does not only depend on the current density j onto the probe collector, but also on the collector's orientation relative to the local beam axis. For this 3D analysis the combined angle from the yaw angle ϕ and the pitch angle ϑ is relevant. This effective angle between probe and thruster α is given by:

$$\alpha = \arctan \frac{\sqrt{(X^2 + Z^2)}}{Y}. \tag{1}$$

Even though both X and Z values can be negative, all values of α from Eq. 1 would be positive. The positive values of α corresponding to negative X are manually set to negative α values to better distinguish the data corresponding to two halves of the ion plume. The coordinate Y is always positive, i.e., it is only negative behind the thruster where no scan is conducted.

Misalignment between probe and thruster decreases the effective collection area, requiring a correction. Additionally, secondary electron emission (SEE) introduces further uncertainty, as emitted electrons are indistinguishable from collected ions in the current measurement. The SEE yield is constant only for small angles but varies for higher incidence angles of the ions onto the collector. This angular dependence is not trivial but can be approximated by the secant of the incidence angle [49, 50]. The ion current density j thus becomes:

$$j = \frac{I}{((A + \kappa_G) \cdot \cos(\alpha))} \cdot \kappa_{\mathrm{SEE}}. \tag{2}$$

with the measured current I, the area of the collector A, the effective increase of the collector area κ_G introduced by ions entering the gap between collector and guard ring, the angle of misalignment or ion incidence angle α, and the SEE correction factor κ_{SEE}. The latter is given by:

$$\kappa_{\mathrm{SEE}} = \frac{1}{1 + \left(\frac{\lambda_{\mathrm{SEE}}}{\cos(\alpha)}\right)}. \tag{3}$$

where λ_{SEE} is the SEE yield which depends on ion species, ion energy, and collector material. Here, for krypton ions at 300 eV onto an aluminum collector, the coefficient is 0.045(10) [51–54].

Another important issue is how well angular misalignment can be corrected. In theory, any deviation can be adjusted mathematically using the angle-dependent collector area and SEE yield correction. However, at large angles, the combined uncertainties arising from alignment, angle measurement, and SEE estimation increase significantly and

determine the accuracy of post-corrected data. This issue is revisited in Section "Uncertainty analysis". At the tails of the angular current density distribution the data is extrapolated to zero.

As shown in Eq. 4 the impact of $j(\alpha)$ scales with $\sin\alpha$, and thus even though the current density falls off rapidly at large α, it should not be neglected. For this reason the data is extrapolated beyond the measurement range. Here the resulting total beam current and divergence effiency was shown to be insensitive to the method of extrapolation and a linear fit to zero is used.

To derive the total beam current, the angle-resolved current-density values need to be integrated [2]. Because the dataset is discrete, a summation is used instead:

$$I_{\mathrm{Beam}} = \pi \sum_{\alpha=-\frac{\pi}{2}}^{\frac{\pi}{2}} j(\alpha) R(\alpha)^2 \sin(\alpha) \Delta\alpha, \tag{4}$$

where R is the distance to the assumed plume origin and $\Delta\alpha$ is the angular bin width. At the tails of the distribution, the current density is linearly extrapolated to zero. Furthermore, by weighing the current density at each angle element by $\cos(\alpha)$, a value for the axial current that leaves the thruster along its main axis can be obtained [2]:

$$I_{\mathrm{Axial}} = \pi \sum_{\alpha=-\frac{\pi}{2}}^{\frac{\pi}{2}} j(\alpha) R(\alpha)^2 \sin(\alpha)\cos(\alpha) \Delta\alpha. \tag{5}$$

By comparing the total beam current with its axial component, the divergence efficiency γ can be calculated:

$$\gamma = \frac{I_{\mathrm{Axial}}}{I_{\mathrm{Beam}}}. \tag{6}$$

The comparison between the measurements employing different positioning and pointing strategies will be based on the quantities I_{Beam} and γ as well as corresponding uncertainties.

In addtion to the analysis in terms of beam profile, divergence effiency and total beam current measurement, we also compare different methods to reconstruct the location and even the shape of the ion origin from the data.

Results and discussion

Plume triangulation measurements

The top and bottom graphs on the right of Fig. 5 show the beam profiles as a function of angle to the beam-normal deduced from the scans in the plane furthest away from the thruster for (L-1) and (S-2) scanning, respectively. Current density values are binned in angle intervals of 2 ˚ only, due to the low effective angle density resulting from constant X steps in the center of the linear planes. This binning size of 2 ˚ is kept constant for all of the post processing. In both cases, the blue symbols are current density values in the plane corresponding to the given angle with respect to the beam normal and the open symbols with the uncertainty bars correspond to the average value for a given angle. Compressing the data into this 2D plot of effective angle vs. current density assumes rotational symmetry of the beam (assumption (ii)). The agreement between the blue

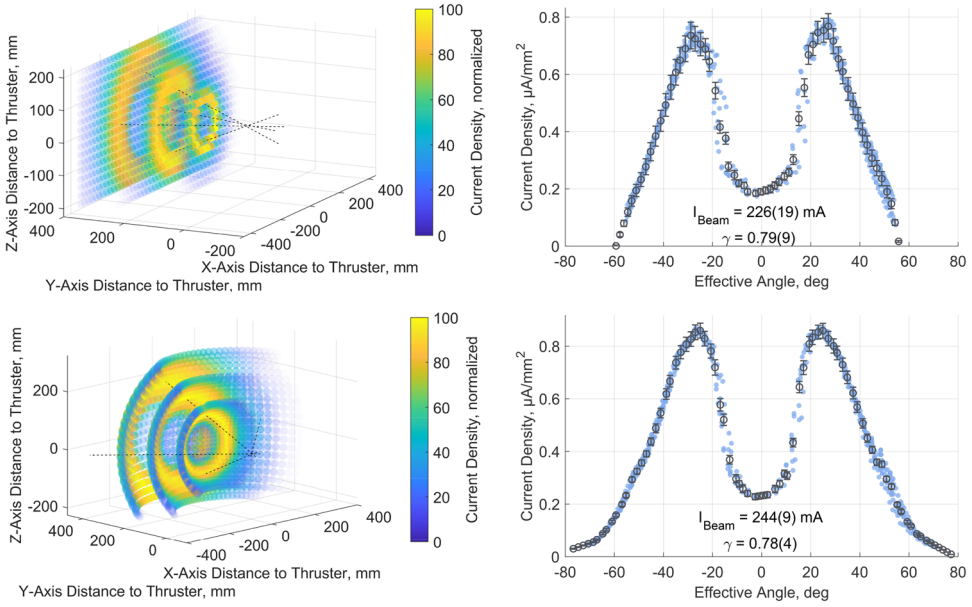


Fig. 5 Top: results beam profile scans following scanning scheme (L-1) based on Cartesian coordinates (see Fig. 1 (C)). The thruster-exit is centered at the origin of the Cartesian coordinate system with the nominal beam direction along the Y-axis. Three scans are performed in the (X,Z) planes at distances of Y = 150 mm, 250 mm, and 350 mm, respectively. left: color-coded 3D plots of the normalized beam current density in each plane. The 3D plots are normalized to better show the plume propagation. The data in X and Z direction is fitted to reveal the location of the maximum and minimum; those positions are traced back in 3D space (dashed lines) to reveal the origin of the plume cone (point-source assumption). right: current density distribution at Y = 350 mm plotted with respect to the angle from the beam normal with respect to the interpolated origin of the plume cone yielding the angular current density distribution for all data points in the corresponding XZ-plane (blue) and the average current density for a given angle (black). bottom: results of the beam profile scans following scanning scheme (S-2) based on spherical coordinates (R,φ,ϑ) which have their origin in the center of the thruster exit plane and the direction ($\varphi = 0$, $\vartheta = 0$) corresponding to the nominal plume direction perpendicular to the thruster exit-plane. Scans were performed in sphere-shells of different radius, i.e., $R = 150$ mm, 250 mm, and 350 mm, but the same origin. left: color-coded 3D plots of the normalized beam current density in each sphere shell. The 3D plots are normalized to better show the plume propagation. The data is fitted to reveal the location of the maximum and minimum; those positions are traced back in 3D space (dashed lines) to reveal the origin of the plume cone (point-source assumption). right: average current density distribution in the third sphere shell with $R = 350$ mm as a function of angle from the beam normal with respect to the interpolated origin of the plume cone, again blue symbols correspond to all data points in the plane and black symbols to the average current density for each angle

symbols and the averaged data points confirm that assumption (ii) is valid for this ACFT. The results of the (L-1) and (S-2) scanning yield the same value of the divergence efficiency within the experimental uncertainties ($\gamma = 0.79(9)$ and $0.78(4)$).

The top and bottom graphs on the left side show two sets of data scanned in three planes. The current in each plane is normalized to its respective maximum. The opacity of the datapoints is scaled with their relative amplitude, to prevent front planes from obscuring back planes. The black dashed lines indicate the triangulation, and the convergence points are compared in Fig. 8. This method converges to within the general accuracy of the gantry of 7.5 mm after one iteration. However, without additional studies, the uncertainty of this method is unclear and needs to be viewed only in the context of the other methods of finding the plume origin.

It is worth noting that the calculated beam current ($I_{\mathrm{Beam}} \approx 240\,\mathrm{mA}$) exceeds the current measured by the power supply ($I_{\mathrm{Anode}} = 237\,\mathrm{mA}$). This indicates a current utilization of $> 100\,\%$, which is likely an artifact of using nude Faraday probes and it depends on facility back-pressure as discussed in Section "Nude Faraday probe". A more realistic

value for the discharge efficiency of this ACFT is $\approx 80\,\%$ [33, 45]. The probe collects low-energy charge-exchange (CEX) ions and is affected by SEE. A subsequent study shows that similar to HTs [2, 17], the nude probe slightly underestimates the current density in the peak of the distribution but significantly overestimates the current everywhere else, leading to a net overestimation of the beam current for ACFTs, particularly in the tails of the distribution [45].

Additionally, a decrease in effective pumping speed was observed between the linear (L) and spherical (S) campaigns, likely due to the onset of cryo-pump and cold trap saturation after a week of testing. This caused the background pressure to rise from 2.3×10^{-5} mbar to 2.9×10^{-5} mbar (nitrogen equivalent), resulting in an approximately 5% rise in measured beam current for the measurements conducted later in the campaign, consistent with previous findings [2, 17, 45]. The anode current, as measured by the power supply, only shows a 1% increase. It is worth pointing out that either measurement analysis is carried out self consistently and the individual results between (L-1), (L-2) and (L-3), as well as between (S-2) and (S-3) are comparable. The difference in background pressure between the L and S sets of measurements is acceptable as the emphasis of this work is our comparison of the pointing schemes 1–3 and less so on the scanning schemes L and S.

Direct comparison between pointing schemes

To compare the different pointing schemes, for both the Cartesian and spherical movement, the gantry performed a line scan at the Z = 0 height of the thruster along a line or semicircle respectively. As with all the other movement schemes, the spatial resolution is given by the 25 mm steps between measurement points in Cartesian movement and by 2 ° steps for spherical measurements. At each position of the linear scan, all three pointing schemes (L-1), (L-2) and (L-3) were employed to allow a direct comparison. The resulting current density profiles with corresponding uncertainties are presented in top graph of Fig. 6. Scanning and pointing scheme (L-1) where the Faraday probe is rigidly mounted and points antiparallel to the Y direction exhibits very large uncertainty at high angles due to the decrease of the effective detection area with $\cos(\alpha)$ and the required correction of the SEE yield. These effects are already remediated in scheme (L-2) where the probe is always pointed at the nominal origin of the assumed point source, i.e., the center of the thruster exit-plane. Corrections for (L-2) are thus only based on the remaining difference between where the thruster was measured to be, and where the triangulation converges. From there, only little improvement is obtained by maximizing the detected ion beam current at each location following pointing scheme (L-3), where no angle correction is necessary.

The situation in the bottom graph of Fig. 6 is somewhat similar. Again only a marginal uncertainty reduction is obtained when employing the pointing scheme (S-3) over (S-2). The reason (S-2) is almost as good as (S-3) is likely that the point source assumption holds sufficiently well as the scan radius ($R = 350$ mm) is significantly larger than the opening diameter of the thruster exit ($d = 35$ mm). Since geometric constraints of the vacuum chamber allow higher angles for spherical measurements than linear ones, more data is captured in the tails, allowing for more accurate extrapolation.

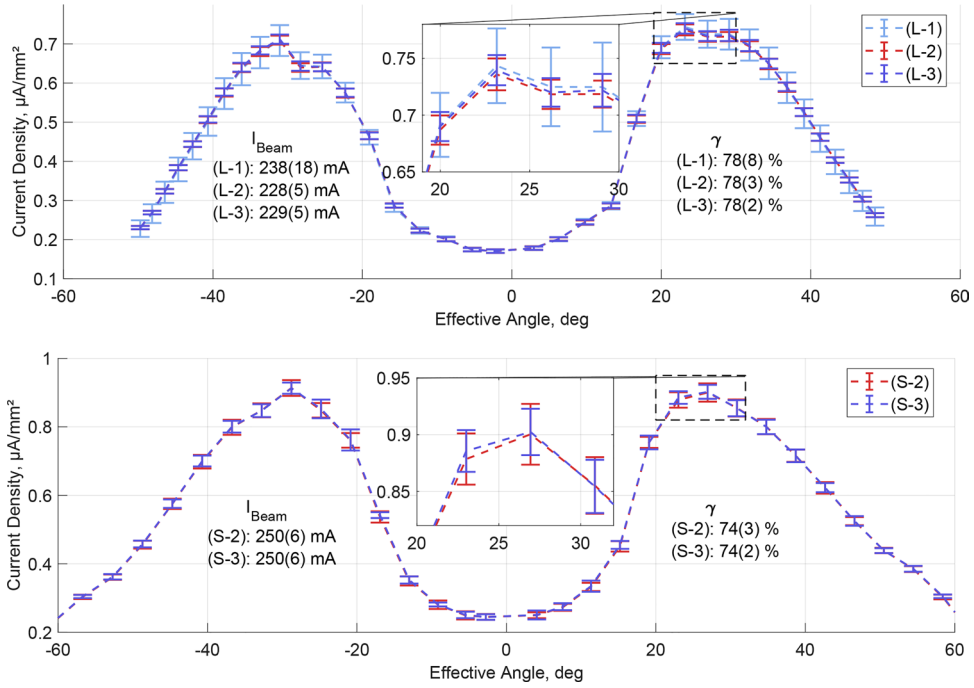


Fig. 6 Top graph: angular current density profiles obtained by the three different pointing schemes in a linear scan along the X direction at constant Y = 350 mm and Z = 0 mm. In the scheme (L-1) the probe points antiparallel to the Y direction. In (L-2) the probe points towards the mechanical measurement of the thruster exit plane and for (L-3) the probe finds the direction of maximum measurable current density. The three measurement strategies are compared in terms of their current density distribution, relative uncertainty as well as the measured total beam current and divergence efficiency. Bottom graph: angular current density profiles obtained by the pointing schemes (S-2) and (S-3) of the Faraday probe in a round scan along a semicircle in the XY-plane with radius $R = 350$ mm with the origin in the center of the thruster exit-plane. In (S-2) the probe points towards the mechanical measurement of the thruster exit plane and for (S–3) the probe finds the direction of maximum measurable current density. The two measurement strategies are compared in terms of their current density distribution, relative uncertainty as well as the measured total beam current and divergence efficiency

Source reconstruction

While using the scans of (L-3) and (S-3) provides little to no benefit for accurately determining the current density profile compared to (L-2) and (S-2), the strength of the scanning and positioning schemes (L-3) and (S-3) with the rotatable Faraday probe is that the main direction of the incoming ion trajectories can be determined locally without having to make any assumptions about the origin of the trajectories. Therefore this dataset contains more information. Fig. 8 illustrates these directions of maximum current obtained in the X-Y plane by using the local orientation of the Faraday probe at each position after current maximization.

The pointing variation is implemented such that the center of the collector surface does not move between two different pointing schemes, as the gantry effectively pivots in such a way that the center of the collector becomes a remote center of rotation. In practice, the correct orientation of the Faraday probe at a given scan location within the plume is the one where the measured current density is at its maximum. Figure 7 shows two examples of the procedure used to determine the local maximum current density value at a given scan position. Details of the procedure are given in the figure caption.

The results demonstrate that the ion trajectories do not possess a common intersection point, but rather exhibit several characteristic point-like areas within the thruster volume. The "bunching" of the lines occurs because the outside scan positions do not

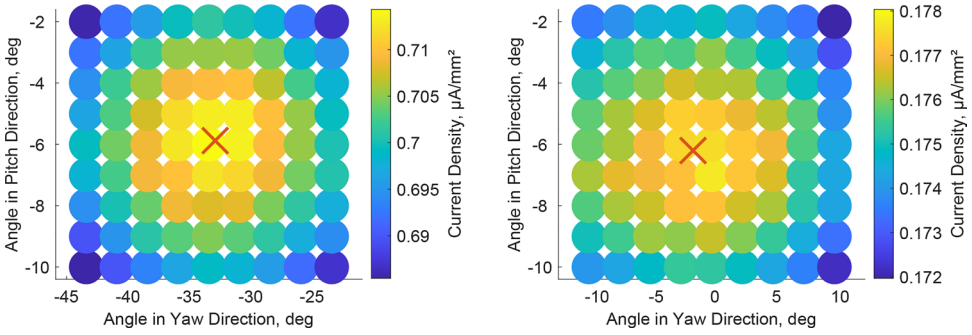


Fig. 7 Results of direction-dependent current density measurements at two different given scan locations within the plasma plume. The data is recorded using a Faraday probe mounted on a gimbal to allow for yaw and pitch angle variation. The angle of the collector normal with respect to the expected ion current direction (given by the mechanically measured center of the thruster exit-plane) is varied on a 9×9 grid in 2.5 ° steps about the anticipated direction. The direction corresponding to the local maximum ion density is determined by fitting the data to a 2nd order polynomial. The result is indicated by a red X in both graphs. Left: Scan position corresponding to a maximum of the ion current density distribution. Right: Scan position corresponding the central dip of the current density distribution

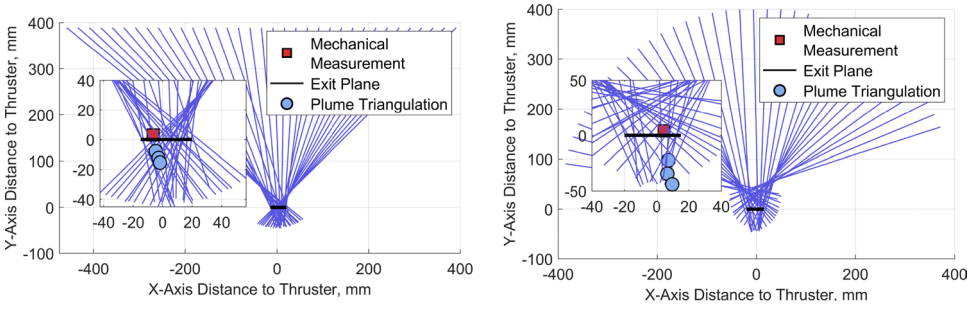


Fig. 8 Results of the local direction dependent current density measurements. From the location of the measurement a line is drawn in the direction of the maximum current. The bunch of lines reveals that the true shape of the plume origin is not a diffuse point source but a 3D object with a stark resemblance of the thruster and its discharge chamber geometry. Furthermore, the location of the assumed exit plane is included in red, the width of this exit plane in black and the locations of the estimated point source by means of beam triangulation convergence are included in light blue. The left and right figure on the left show results of the L and S scan, respectively

have a direct line of sight to the center of the discharge chamber, causing the vectors to converge at the corners of the chamber. The resulting shape effectively projects the thruster discharge volume.

Here, the uncertainty of the direction is omitted. The base uncertainty of the gantry would allow distinguishing between two positions which are 7.5 mm apart. This dimension is indicated by the size of the icons. Technically, the lines in Fig. 8 would have to be as wide as the collector dimension and its pointing accuracy, which would be on the order of the size of the icons. The fact that the resulting shape projected by the lines then closely resembles the shape and dimension of the discharge chamber can be considered to emerge despite the uncertainty of the gantry.

The "Source Positions" listed in Table 1 are therefore calculated as the geometric center of this effective thruster volume. It is also clear that the exit plane is only a crude approximation for the point source location. This result can already be seen by only looking at the results of the plume triangulation method. It turns out that, in both cases, (L-1) and (S-2) the assumption that the origin of the center of the thruster exit-plane, the mechanical measurement, coincides with the intersection point of the back-traced

Table 1 Table of all results of the different probe positioning and pointing schemes. Linear planes refers to the measurements along cartesian coordinates, as shown in the top of Fig. 5, linear line refers to the measurement along a single Z height where the different methods are directly compared as shown in the top of Fig. 6. Spherical planes refers to the measurements along spherical coordinates, as shown in the bottom of Fig. 5, spherical line refers to the measurement along a single Z height where the different methods are directly compared as shown in Fig. 6. All locations are relative to the gantry origin and can be compared against the measured values of location and current consumption in the last row

Method, direction pointing	Y Pos of source, mm	X Pos of source, mm	Z Pos of source, mm	Beam current I_{Beam}, mA	Divergence efficiency γ, %
Linear Planes					
Y Dist: 150 mm	–54	507	210	253(49)	76(20)
Y Dist: 250 mm				247(29)	77(12)
Y Dist: 350 mm				226(19)	79(9)
Linear line					
Straight, corr. by triangulation	–54	507	210	238(18)	78(8)
Mechanical measurement	–36	504	200	228(5)	78(3)
Angular current maximum	–40	499	204	229(5)	78(2)
Spherical Planes					
Dist.: 150 mm	–88	509	206	261(12)	84(6)
Dist.: 250 mm				252(10)	80(5)
Dist.: 350 mm				244(9)	78(4)
Spherical line					
Mechanical measurement	–36	504	200	250(6)	74(3)
Angular current maximum	–40	505	211	250(6)	74(2)
Mechanical Measurement/ Power Supply	–36	504	200	237	

ion trajectories does not hold. In both cases, the point of origin found is behind the exit plane inside the thruster. This is consistent with the assumption that the ions leave the virtual grid anywhere in the exit plane and are then accelerated away as discussed in Section "Advanced Cusp Field Thruster" and Fig. 2. Essentially, this means that the assumption of a point source at the center of the exit plane of the thruster is usually not correct. The iterative process of triangulating the plume source origin is shown with the light blue circles in Fig. 8. Here, the red square represents the mechanical measurement and the black line shows the dimension of the thruster exit, superimposed onto the thruster-like shape of the lines, the sizes of the icons represent their uncertainty of ≈7.5 mm.

Diagnostic implications

The comparison of different scanning and positioning schemes demonstrates that, in theory, even large angle deviations can be corrected for when using a rigid Faraday probe. However, in a scheme where the probe moves along a Cartesian axis parallel to the thruster exit-plane, the measurement uncertainty disproportionately increases towards large incidence angles.

In contrast, the relative accuracy between thruster and probe positioning does not need to be better than 7.5 mm for distances between 300 and 500 mm in the case of a semi-circular measurement path. Here, the pointing accuracy is natively within 1° to 2° towards the center of the thruster exit-plane. In this case, the measurement of current itself becomes the dominant factor of uncertainty, rather than the geometric alignment. Therefore, the commonly used spherical C-shaped scanner arrays are sufficiently accurate if the point source assumption is justified (large $R : d$ ratios). However, for near-field

measurements or thrusters without rotational symmetry, the rotatable probe (L-3/S-3) is required to resolve the volumetric nature of the source.

The results of all measurement strategies, when analyzed self-consistently, are presented in Tab. 1. The table contains the resulting point-source location as well as the values for I_{Beam} and γ. As discussed, the spherical measurements have an approximate increase in the current density of 5% as a result of higher background pressure and we recommend no direct comparison between the round and the linear measurement strategies. The locations are given in reference to the gantry origin which coincides with the center of the thruster exit-plane which is the nominally assumed origin of the ion trajectories following the point source assumption.

Uncertainty analysis

Total measurement uncertainty arises from the uncertainty of the current density measurement j, the uncertainty of the determination of the distance R, the uncertainty of the angle between thruster and collector α and the SEE yield $\kappa_{\mathrm{SEE}}(\alpha)$ coefficient. We assume all variables to have independent causes of uncertainty and the propagation of uncertainty then yields values for the total beam current I as well as the divergence efficiency γ.

Three different pointing schemes have been employed for the ion-current density-profile measurements in the scans along Cartesian coordinates, i.e., (L-1) with a rigid probe oriented perpendicular to the scanning direction and antiparallel to the nominal plume direction, (L-2) where the probe at each location is pointed towards the assumed point source center, i.e., the center of the thruster-emitter plane, and (L-3) where the probe at each location is oriented such that the measured current signal is maximum. The pointing schemes in spherical schemes (S-2) and (S-3) are essentially the same as those in (L-2) and (L-3), respectively. Therefore, our discussion of the total measurement uncertainty obtained by error propagation and its contributions will only focus on the three linear schemes (L-1), (L-2) and (L-3).

The uncertainty analysis of the three scanning schemes is based on the ion-current density-profile measurements shown in the top graph of Fig. 6. In all measurements independent of the scanning scheme, the relative standard deviation of the measured current value is about 1% of its absolute value and can be considered a base line.

In the (L-1) scheme, the primary source of uncertainty is the angle between probe position and the normal direction of the exit plane of the thruster. This angle is important, since the effective collector surface area as well as the SEE yield depend on it. Its uncertainty is given by the uncertainties of the X and Y coordinate of the origin of the point. Here we use the uncertainty of the gantry to thruster positioning itself, where the conservative estimate from Section "Experimental setup" yields 7.5 mm. The impact due to the angle uncertainty makes the contribution due to corrections of the effective collector surface area and the SEE factor dominant at large angles. This shows that the (L-1) scheme works best on thrusters with a small divergence angle such as GITs and should be avoided for other ion sources, if low uncertainty is required. This uncertainty, both absolute and relative values is presented in Fig. 9. Here, we present the individual contributions of the source meter used for current measurements, the impact of the effective collector area itself as well as the impact of the SEE yield correction.

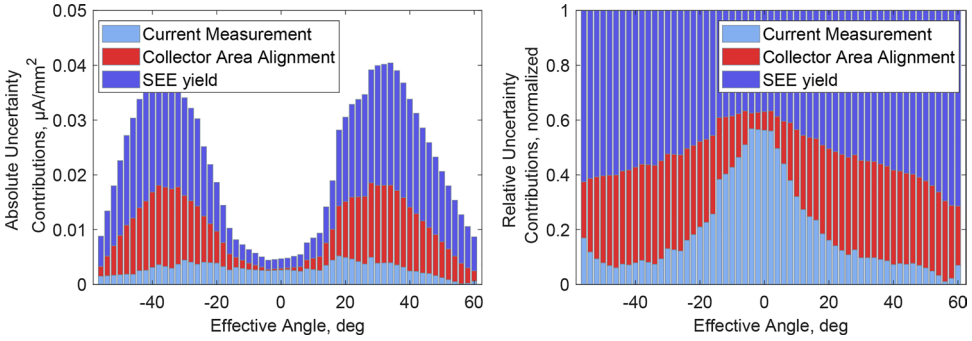


Fig. 9 Two plots showing the angle dependence of measurement uncertainty of measurement scheme (L-1) (along cartesian coordinates with the probe pointing straight forward) the figure on the left shows the absolute contribution towards the measurement uncertainty, and the figure on the right shows the relative uncertainty where each angle bin is normalized to 1. The measurement uncertainty introduced by the current density measurement itself, while dominant in the center region, loses relevance towards the edges of the current distribution. Where the contribution of the collector alignment heavily impacts the uncertainty of the correction for the SEE yield and the effective area of the collector

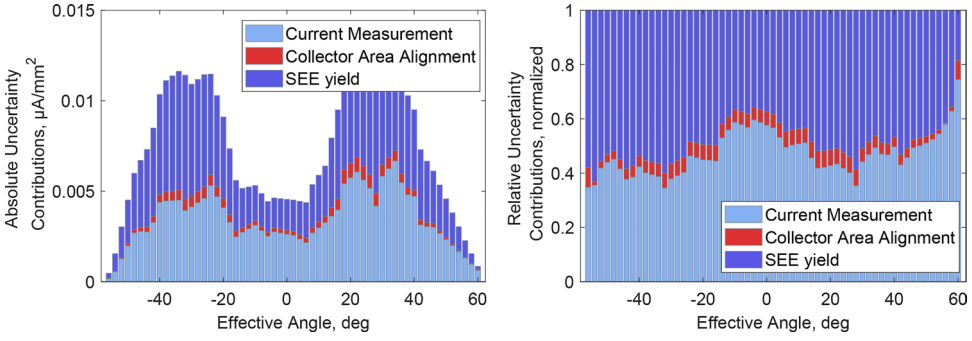


Fig. 10 Angle dependence of measurement uncertainty of an ion-current density-profile measurement following the positioning and pointing scheme L2. Left: absolute contributions towards the measurement uncertainty, right: relative uncertainty where each angle bin is normalized to 1. The measurement uncertainty introduced by the current density measurement itself contributes about half of the total measurement uncertainty, while the contribution due to collector alignment is negligible

The relationship between the electrical measurement uncertainty and the uncertainty due to geometric considerations completely changes, once the probe is pointed towards the thruster, whose location is measured before pump down. After post processing the data and finding the center of the plume from three planar measurements (see top of Fig. 5) these values are corrected to reflect this actual position of the plume source. It becomes immediately obvious that the uncertainty of the collector surface correction as shown in Fig. 10 is now negligible. The correction factor for the SEE now shares the total uncertainty contribution with the electrical measurement by the source meter. The SEE correction factor used is 0.045(10). This uncertainty could be improved by using a propellant - material combination where this material parameter is better known. The stepper motors were the limiting factor for the analog current measurement, even though both the motor wires and the wire between collector and source meter were in shielded and grounded co-axial wires. Due to the long harness of the gantry and the close proximity of these wires inside the harness we were not able to suppress the noise past 1%, while the Keithley 2401 source meter has an intrinsic accuracy one to two orders of magnitude higher, depending on the amplitude.

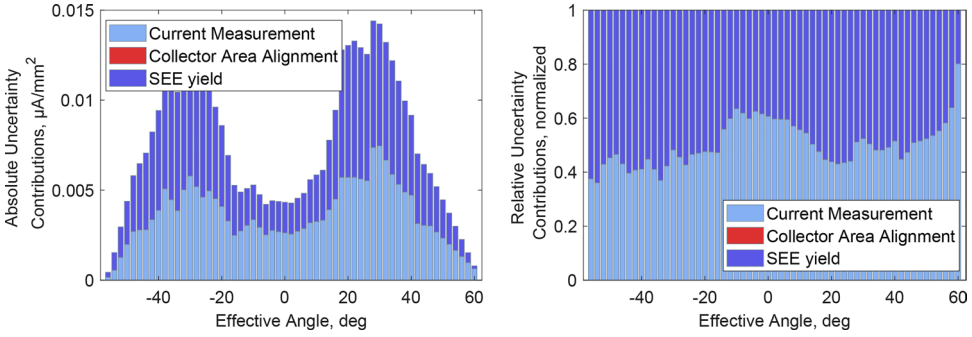


Fig. 11 Angle dependence of measurement uncertainty of an ion-current density-profile measurement following the positioning and pointing scheme L-3. Left: absolute contributions towards the measurement uncertainty, right: relative uncertainty where each angle bin is normalized to 1. The measurement uncertainty introduced by the current density measurement itself now contributes half of the total measurement uncertainty, while the contribution due to collector alignment has now vanished

Lastly, the uncertainty of the current maximization technique is shown in Fig. 11. Here, we need to assume that no angular misalignment is present, affecting both the collector area and the SEE yield due to the lack of incidence angle uncertainty. As is clear by comparing the values from Figs. 10 and 11 as well as comparing the resulting current density profiles as shown in Fig. 6, eliminating the last remaining uncertainty regarding pointing angle of the probe shows a negligible effect. Especially considering the increase of the mechanism complexity.

Conclusion

We built a gantry system with five degrees of freedom consisting of three translatory axes for varying the Faraday probe location on a Cartesian grid as well as two motorized axes for yaw and pitch angle rotation for pointing the probe's orientation. This allowed us to directly compare five different scanning and positioning schemes for measuring ion-current density profiles of an ACFT under nearly identical experimental conditions.

The measured data has been compared and assessed. As long as the assumption that the thruster acts as a point source can be justified (i.e., the distance R between Faraday probe and detector is much larger than the extension of the thruster exit-plane d), the ion-current density-profiles obtained by the different scanning schemes are the same within the experimental uncertainties. Our experiments were performed at an $R : d$ ratio of $10 : 1$. Already in this range, scanning and positioning schemes with the rotatable Faraday probe exhibit the smallest measurement uncertainties and are independent of the point-source assumption.

A key result is that commonly used spherical C-shaped scanner arrays are sufficiently accurate if the point source assumption is justified. There is little gain in accuracy by actively aligning the probe to the direction of maximum current.

By adding probes in the central $\vartheta = 0$ plane at different radii, additional certainty for the plume's origin and beam propagation can be gained with minimal additional complexity, as this allows plume triangulation via measurements in three radii. This forms the basis for the plasma diagnostic system of the new iodine kW propulsion research facility at Airbus Friedrichshafen.

However, a major advantage of schemes employing a rotatable Faraday probe is the possibility of locally determining the ion beam direction by rotating the probe

orientation to the maximum current signal. This allows one to generate a map of the points within the thruster volume from which the ion trajectories seem to originate. These maps may prove useful for optimizing discharge vessels of ion thrusters in the future. Furthermore, our results suggest that scanning and positioning schemes with a rotatable Faraday probe are required for assessing ion plume profiles in cases where the point source assumption is no longer valid, such as characterizing larger thrusters in small vacuum chambers or characterizing clusters of thrusters.

This publication highlights that measurement uncertainty is a critical factor for any positioning and pointing scheme used in ion-current density-profile measurements and should, therefore, always be discussed. Specifically, for the purposes of developmental research, the uncertainty of plume measurements may be on the same order of magnitude as potential incremental improvements between two research prototype thrusters [40–42, 44]. While the measurement uncertainty is sometimes presented as part of the data [4, 14–17] it is usually completely omitted [3, 5–13, 18–26].

Acknowledgements
The authors would like to thank the participating team at Airbus Friedrichshafen.

Author contributions
L.B. wrote the main manuscript. L.B. conducted the experiments, analysis and prepared the figures. All authors reviewed the manuscript and provided feedback.

Funding
Open Access funding enabled and organized by Projekt DEAL. This project has received funding from the European Union's Horizon 2020 research and innovation program under grant agreement No. 870336.

Data availability
The telemetry data from the gantry and the laboratory test equipment is available, as well as the figures as full resolution/vector graphics: https://doi.org/10.22029/jlupub-20187

Declarations

Ethical approval
Not applicable.

Consent
Not applicable.

Competing interests
The authors declare no competing interests.

Received: 18 September 2025 / Accepted: 30 January 2026
Published online: 30 January 2026

References

1. Goebel DM, Katz I (2008) Fundamentals of Electric Propulsion. John Wiley & Sons, Inc, Hoboken, NJ, USA. https://doi.org/10.1002/9780470436448
2. Brown DL, Walker ML, Szabo J, Huang W, Foster JE (2017) Recommended practice for use of faraday probes in electric propulsion testing. J Propul Power 33(3):582–613. https://doi.org/10.2514/1.b35696
3. Holste K, Dietz P, Scharmann S et al (2020) Ion thrusters for electric propulsion: scientific issues developing a niche technology into a game changer. Rev Sci Instrum 91(6):061101
4. Bauer L, Vaupel M et al (2022) Advanced Cusp Field Thruster upscaling with alternative scaling schemes. In: 8th Edition of the Space Propulsion Conference, 3AF, Estoril, Portugal
5. Bauer L, Vaupel M, Blättermann H, Hey FG, Klar PJ (2025) Effects of a magnetic discontinuity in a modified Advanced Cusp Field Thruster. J Electric Propul 4(55). https://doi.org/10.1007/s44205-025-00155-9
6. Loeb HW, Schartner KH, Meyer BK, Feili D, Weis S, Kirmse D (2005) Forty years of giessen ep-activities and the recent rit-microthruster development. In: The 29th International Electric Propulsion Conference, Electric Rocket Propulsion Society, Princeton, USA
7. Touzeau M, Prioul M, Roche S, Gascon N, Pérot C, Darnon F, Béchu S, Philippe-Kadlec C, Magne L, Lasgorceix P et al (2000) Plasma diagnostic systems for hall-effect plasma thrusters. Plasma Phys Control Fusion 42(12B). https://doi.org/10.1088/0741-3335/42/12b/324
8. Bundesmann C, Eichhorn C, Scholze F, Spemann D, Neumann H, Pagano D, Scaranzin S, Scortecci F, Leiter HJ, Gauter S et al (2016) An advanced electric propulsion diagnostic (aepd) platform for in-situ characterization of electric propulsion thrusters and ion beam sources. Eur Phys J D 70(10):e2016. https://doi.org/10.1140/epjd/-70236-0

9. Bundesmann C, Tartz M, Scholze F, Leiter HJ, Scortecci F, Gnizdor RY, Neumann H (2010) Note: An advanced in situ diagnostic system for characterization of electric propulsion thrusters and ion beam sources. Rev Sci Instrum 81(4). https://doi.org/10.1063/1.3386585
10. Bundesmann C, Scholze F, Eichhorn C, Spemann D, Neumann HFS, Leiter HJ, Holste K, Klar PJ (2017) Development of advanced in-situ ep diagnostic tools at iom: current status. In: The 35th International Electric Propulsion Conference, Electric Rocket Propulsion Society, Atlanta, USA
11. Lim JW, Huang SY, Xu L, Yee JS, Sim RZ, Zhang ZL, Levchenko I, Xu S (2018) Automated integrated robotic systems for diagnostics and test of electric and micropropulsion thrusters. IEEE Trans Plasma Sci 46(2):345–353. https://doi.org/10.1109/tps.2018.2795023
12. Zhang Z, Zhang Z, Xu S, Ling WY, Ren J, Tang H (2021) Three-dimensional measurement of a stationary plasma plume with a faraday probe array. Aerosp Sci Technol 110:106480. https://doi.org/10.1016/j.ast.2020.106480
13. Huang W, Shastry R, Soulas GC, Kamhawi H (2013) Farfield plume measurement and analysis on the nasa-300m and nasa-300ms. In: The 33th International Electric Propulsion Conference, Electric Rocket Propulsion Society, Washington DC, USA
14. Mühlich NS, Gerger J, Seifert B, Aumayr F (2022) Simultaneously measured direct and indirect thrust of a feep thruster using novel thrust balance and beam diagnostics. Acta Astronautica 197:107–114. https://doi.org/10.1016/j.actaastro.2022.05.009
15. Bock D, Laufer P, Paries F, Kopnarski M, Tajmar M (2017) Plume characterization of nanofeep thrusterswith a plasma diagnostics facility using carbon-velvet probes. In: The 35th International Electric Propulsion Conference, Electric Rocket Propulsion Society, Atlanta, USA
16. Habl L, Rafalskyi D, Lafleur T (2020) Ion beam diagnostic for the assessment of miniaturized electric propulsion systems. Rev Sci Instrum 91(9):093501. https://doi.org/10.1063/5.0010589
17. Frieman JD, Brown NP, Liu CY, Liu TM, Walker ML, Khayms V, King DQ (2018) Electrical facility effects on faraday probe measurements. J Propul Power 34(1):267–269. https://doi.org/10.2514/1.b36467
18. Bonelli E, Scaranzin S, Scortecci F, Saito F, Killinger R, Kukies R, Leiter H (2005) A 3.000 hours endurance testing of rit-22 thruster in the new aerospazio test facility. In: The 29th International Electric Propulsion Conference, Electric Rocket Propulsion Society, Princeton, USA
19. Scholze F, Bundesmann C, Eichhorn C, Spemann D (2019) Determination of the beam divergence of a gridded ion thruster using the aepd platform. In: The 36th International Electric Propulsion Conference, Electric Rocket Propulsion Society, Vienna, Austria
20. Hey FG, Vaupel M, Groll C, Tajmar M (2017) Development of a gridless retarding potential analyser. In: The 35th International Electric Propulsion Conference, Electric Rocket Propulsion Society, Atlanta, USA
21. Neumann A (2017) Stg-et: dlr electric propulsion test facility. J Large-Scale Res Facil JLSRF 3. https://doi.org/10.17815/jlsrf-3-156
22. Brown DL, Gallimore AD (2009) Evaluation of plume divergence and facility effects on far-field faraday probe current density profiles. In: The 31th International Electric Propulsion Conference. Electric Rocket Propulsion Society, Ann Arbor, USA
23. Brown DL, Gallimore AD (2010) Evaluation of ion collection area in faraday probes. Rev Sci Instrum 81(6). https://doi.org/10.1063/1.3449541
24. Benavides GF, Mackey J, Ahern D, Thomas R. Diagnostic for verifying the thrust vector requirement of the AEPS hall-effect thruster and comparison to the NEXT-C thrust vector diagnostic. https://doi.org/10.2514/6.2018-4514
25. Reijen B, Weis S et al (2013) High precision thrust vector determination through full hemispherical rpa measurements assisted by angular mapping of ion energy charge state distribution. In: The 33th International Electric Propulsion Conference, Electric Rocket Propulsion Society, Washington DC, USA
26. Hofer RR, Walker M, Gallimore AD (2001) A comparison of nude and collimated faraday probes for use with hall thrusters. In: The 27th International Electric Propulsion Conference, Electric Rocket Propulsion Society, Pasadena, USA
27. Désangles V, Packan D, Jarrige J, Peterschmitt S, Dietz P, Scharmann S, Holste K, Klar PJ (2023) Ecra thruster advances: 30w and 200w prototypes latest performances. J Electric Propul 2(1). https://doi.org/10.1007/s44205-023-00046-x
28. Blättermann H et al. (2024) Endurance testing and characterization of a novel candidate for CubeSat propulsion: the Advanced Cusp Field Thruster (ACFT). Acta Astronautica. https://doi.org/10.1016/j.actaastro.2024.03.074
29. Leiter H, Killinger R, Boss M, Braeg R, Gollor M, Weis S, Feili D, Tartz M, Neumann H, Cara DM RIT-μX - high precision micro ion propulsion system based on RF-technology. https://doi.org/10.2514/6.2007-5250
30. Kottke N, Bauer L, Becke P et al (2024) Development of an iodine fed Advanced Cusp Field Thruster for mid-Power–iFACT-MP. In: The 38th International Electric Propulsion Conference, Electric Rocket Propulsion Society, Toulouse, France
31. Frieman JD, Walker JA, Walker MLR, Khayms V, King DQ (2016) Electrical facility effects on hall thruster cathode coupling: performance and plume properties. J Propul Power 32(1):251–264. https://doi.org/10.2514/1.B35683
32. Walker JA, Langendorf SJ, Walker MLR, Khayms V, King D, Pertson P (2016) Electrical facility effects on hall current thrusters: electron termination pathway manipulation. J Propul Power 32(6):1365–1377. https://doi.org/10.2514/1.B35904
33. Vaupel M, Kottke NG et al (2022) Iodine fed Advanced Cusp Field Thruster endurance test results. In: 8th Edition of the Space Propulsion Conference, 3AF, Paris, France
34. Keller A, Köhler P, Hey FG et al (2013) Parametric study of HEMP-Thruster, downscaling to µN thrust levels. In: The 33rd International Electric Propulsion Conference, Electric Rocket Propulsion Society, Washington DC, USA
35. Hey FG (2018) Micro Newton thruster Development. Springer, Heidelberg, Germany. 978-3-319-96177-4
36. Janes GS, Wilson T (1962) Electrostatic acceleration of neutral plasmas - momentum transfer through magnetic fields. In: Proceedings of the Third Symposium on Advanced Propulsion Concepts
37. Kornfeld G, Koch N, Coustou G (2003) The highly efficient multistage plasma (HEMP) thruster, a new electric propulsion concept derived from tube technology. In: Fourth IEEE International Vacuum Electronics Conference
38. Courtney DG, Martinez-Sanchez M (2007) Diverging cusped-Field hall thruster (DCHT). In: 30th International Electric Propulsion Conference, Electric Rocket Propulsion Society, Florence, Italy
39. Hey FG, Vaupel M, Kottke NG et al (2022) Overview of the European iodine Fed Cusp Field thruster research and innovation action - iFACT. In: The 37rd International Electric Propulsion Conference, Electric Rocket Propulsion Society, Cambridge, USA

40. Hey FG, Vaupel M et al (2019) Inter-laboratory comparison: tests of a single thruster in two different facilities, on two different thrust balances. In: The 36rd International Electric Propulsion Conference, Electric Rocket Propulsion Society, Vienna, Austria
41. Vaupel M, Hey FG et al (2015) The next generation milli-Newton µHEMPT as potential main thruster for small satellites. In: The 35rd International Electric Propulsion Conference, Electric Rocket Propulsion Society, Atlanta, USA
42. Vaupel M, Kottke NG et al (2021) Development status of the Advanced Cusp Field Thruster propulsion system. In: 7th Edition of the Space Propulsion Conference, 3AF, Paris, France
43. Vaupel M et al (2018) Performance of the mN-HEMPT with iodine and xenon. In: 6th Edition of the Space Propulsion Conference. 3AF, Seville, Spain
44. Vaupel M et al (2019) Characterisation and performance comparison of a low-Power hall-effet thruster and an Advanced Cusp Field Thruster with multiple noble gases. In: The 35rd International Electric Propulsion Conference, Electric Rocket Propulsion Society, Vienna, Austria
45. Blättermann H, Bauer L et al. (2026) Design improvements and performance Evaluation of a gridless retarding potential analyzer (gRPA) for EP plume diagnostics. J Electric Propul
46. Liu H, Niu X, Li X, Yu D (2020) Simulation study of influence of exit magnetic separatrix angle on plume divergence control. Eur Phys J D 74(10). https://doi.org/10.1140/epjd/e2020-100595-0
47. ISO 2768-1:1989-11, General tolerances; part 1: tolerances for linear and angular dimensions without individual tolerance indications
48. Dankanich JW, Walker M, Swiatek MW, Yim JT (2017) Recommended practice for pressure measurement and calculation of effective pumping speed in electric propulsion testing. J Propul Power 33(3):668–680. https://doi.org/10.2514/1.b35478
49. Ohya K (1992) Deviation from the inverse cosine law upon incident angle dependence of secondary electron emission from solids under electron and proton bombardments. J Phys Soc Jpn 61(8):3013–3014. https://doi.org/10.1143/jpsj.61.3013
50. Qi-Liang L, Zhu-Ying Z, Li-Qun S, Guo-Qing Z (2005) Incident angle dependence of secondary electron emission from carbon induced by swift h2+. Chin Phys 14(7):1465–1470. https://doi.org/10.1088/1009-1963/14/7/035
51. Alonso EV, Baragiola RA, Ferrón J, Jakas MM, Oliva-Florio A (1980) Z1 dependence of ion-induced electron emission from aluminum. Phys Rev B 22(1):80–87. https://doi.org/10.1103/physrevb.22.80
52. Hagstrum HD (1956) Auger ejection of electrons from tungsten by noble gas ions. Phys Rev 104(2):317–318. https://doi.org/10.1103/physrev.104.317
53. Seah MP (1981) Pure element sputtering yields using 500–1000 ev argon ions. Thin Solid Films 81(3):279–287. https://doi.org/10.1016/0040-6090(81)90490-9
54. Yamauchi Y, Shimizu R (1983) Secondary electron emission from aluminum by argon and oxygen ion bombardment below 3 kev. Jpn J Appl Phys 22(4A). https://doi.org/10.1143/jjap.22.l227

Publisher's Note

Springer Nature remains neutral with regard to jurisdictional claims in published maps and institutional affiliations.